AIChE WILEY InterScience DISCOVER SOMETHING GREAT

REACTORS, KINETICS, AND CATALYSIS

Multiscale Modeling of Turbulent Combustion and NO_x Emission in Steam Crackers

A. Habibi and B. Merci
Dept. of Flow, Heat and Combustion Mechanics, Ghent University-UGent, Ghent, Belgium

G. J. Heynderickx
Laboratory for Petrochemical Engineering, Ghent University-UGent, Ghent, Belgium

DOI 10.1002/aic.11243
Published online July 16, 2007 in Wiley InterScience (www.interscience.wiley.com).

A 3D RANS simulation of lean premixed turbulent combustion in an industrial scale steam cracking furnace is performed. Turbulence is represented by a renormalization group (RNG) $k - \varepsilon$ model, while combustion is modeled with a skeletal mechanism. The eddy dissipation concept (EDC) model is used to account for turbulence/combustion interaction. The turbulent combustion regime is identified as a "thin flame regime with pockets" or a "corrugated flamelet regime". A weighted sum of gray gases model (WSGGM) is used to account for the gas radiative properties. The radiative transfer equation is solved using the P-1 and discrete ordinates method in the conservative finite volume formulation. NO_x calculations are performed as a postprocessing step, with the flow field, temperature, and species concentrations fixed. The formation of NO through thermal, prompt, and N_2O intermediate mechanisms is considered. The in situ adaptive tabulation technique is used to decrease the computational time required to treat the combustion chemistry. The effect of radiation models on the predicted furnace wall, tube skin, and flue gas temperature profiles and heat fluxes toward the reactor tubes, as well as on the predicted species and NO concentration profiles and structure of the furnace flames under normal firing conditions, is discussed. © 2007 American Institute of Chemical Engineers *AIChE J,* 53: 2384–2398, 2007
Keywords: CFD, turbulent premixed combustion, renormalization group, skeletal scheme, radiation, eddy dissipation concept, NO_x modeling

Introduction

Large, gas-fired furnaces are extensively used for steam cracking of hydrocarbons. The furnace is heated by means of gas-fired long flame burners distributed in the furnace floor and/or by means of radiation burners in the furnace side walls. The process gas flows through tubular reactor coils suspended in the furnace. The cracking reactions are highly endothermic and the process gas conversion and product yields are strongly affected by the residence time in the tubes and the temperature profiles in the furnace. Owing to the complex nature of the cracking reactions, accurate predictive simulation tools are required to achieve the best design of steam crackers. For a furnace with long flame burners, a coupled simulation approach is developed by Heynderickx et al.,[1] Oprins et al.,[2] and Oprins and Heynderickx.[3]

In the configuration under study the furnace is heated by long flame burners and fuel and air are premixed before entering the furnace. The reacting flow regime is turbulent. Combustion takes place in a flame front propagating into the unburnt reactants. As such, premixed combustion can be considered as a thin, propagating flame that is stretched and contorted by turbulence. For subsonic flows, the over-

Correspondence concerning this article should be addressed to B. Merci at bart.merci@ugent.be.

all rate of propagation of the flame is determined by both the laminar flame speed and the turbulent eddies. To capture the laminar flame speed, the detailed chemical kinetics, the molecular diffusion processes, and the internal flame structure would need to be resolved. Turbulent premixed combustion can then be described as the interaction between a flame front (thickness δ_T and laminar flame speed S_L) and an ensemble of eddies representing turbulence. These eddies have sizes ranging from the Kolmogorov to integral scales[4,5] and characteristic speeds ranging from the Kolmogorov velocity to the integral RMS of the velocity fluctuations (u'). Turbulence wrinkles and stretches the propagating laminar flame sheet, increasing the sheet area and the effective flame speed. The large turbulent eddies tend to wrinkle and corrugate the flame sheet while the turbulent eddies smaller than the laminar flame thickness (δ_T) may penetrate into the flame sheet and modify the laminar flame structure. Consequently, the turbulent flame speed, which is to be modeled, is influenced by both the laminar flame speed and the turbulence. The analysis of premixed combustion leads to the so-called turbulent combustion diagram where various combustion regimes are identified and delineated by introducing dimensionless characteristic numbers.[6–8]

In the present work, the Reynolds averaged Navier-Stokes (RANS) approach is followed to model turbulence. Given the strong nonlinear nature of the reaction rate expressions with respect to the state variables, closure of the average species reaction rates based on mean values of temperature and species concentrations leads to poor predictions of the reaction source term in the energy equation.[5] Capturing the effect of turbulence on the average reaction rates is an important issue of combustion modeling. Here, the eddy dissipation concept (EDC)[9] in combination with a skeletal combustion mechanism is applied to account for the turbulence/chemistry interaction. Based on the EDC model, the molecular mixing takes place in concentrated isolated regions that occupy a small fraction of the total volume of the reacting fluid. These regions are occupied by fine structures whose characteristic dimensions are in the order of the Kolmogorov microscale. It assumes that reaction occurs in the fine structures.

Since radiation is typically the most significant mode of heat transfer to the cracking coils in the furnace, it must be accurately described. It was shown by Habibi et al.[10] that the P-1 model[11,12] and the discrete ordinates method (DOM) in conservative formulation[13] are well suited to solve the radiative transfer equation (RTE). In that paper, the turbulence/chemistry interaction was modeled by the eddy break-up model (EBU) along with a finite rate dissipation kinetic switch. At the same time, the Rosseland[14] radiation model was shown to perform poorly. The differences in model behavior are due to temperature differences near the burner, activating the chemical reactions and leading to a further temperature rise. As a result the reaction zone is positioned too close to the burner when the Rosseland model is used. This has been confirmed when using the EDC model, but the results are not shown for the sake of brevity.

The emission of pollutants is influenced by the radiative heat transfer from the flames, through the effect on temperature. The prediction of NO_x formation is very sensitive to the temperature and composition fields. Although turbulence–radiation interaction can be important, we do not consider this in the present study. In order to reduce the emissions levels, modern combustion devices are designed to operate close to the lean combustion limit. Combustion proceeds at lower temperature due to excess air and therefore the NO_x emission is considerably reduced. Modeling of the NO_x formation helps to determine the main sources of NO_x and to design the NO_x control measures for steam cracking furnaces.

In this work, a 3D numerical simulation of turbulent reacting flow in the radiation section of an industrial scale steam cracking furnace is performed. NO_x formation is computed in a postprocessing step, with the flow field, temperature, and species concentrations fixed. Prediction of NO_x using this approach is justified based on the fact that the concentrations and formation rates of NO_x reactions are very low and have negligible impact on the results of combustion calculation. The formation of NO can be attributed to three mechanisms: thermal NO, prompt NO, and intermediate NO from N_2O. Here, the impact of the reburning mechanism on NO reduction is also considered.

The goal of this work is thus to combine turbulent flow calculations with detailed combustion chemistry and detailed radiation models, in order to quantify the effect on the calculated flow, temperature, and species concentration profiles in steam cracking furnaces. A flow model capable of predicting correct temperature profiles in furnaces will seriously reduce the simulation time required for coupled furnace calculations,[1,2] facilitating the optimization of the furnace and its operating conditions. Validation of the models has to be performed based on a coupled furnace calculation that provides process gas conversion and product yields, or based on furnace run length simulations.[15] In this work, only furnace segments are simulated to reduce the calculation time needed for the comparison of models.

Modeling Approach

Turbulence modeling

The compressible formulation of RANS equations closed with the renormalization group (RNG) $k - \varepsilon$ model is applied.[16] The rationale behind this choice is explained by Habibi et al.[10] The steady state equations are as follows:

Continuity Equation:

$$\frac{\partial \langle \rho u_i \rangle}{\partial x_i} = 0 \tag{1}$$

Momentum Equation:

$$\frac{\partial \langle \rho u_i \rangle \langle u_j \rangle}{\partial x_j} = -\frac{\partial \langle p_{\text{eff}} \rangle}{\partial x_i} + \frac{\partial}{\partial x_j}\left[\mu_{\text{eff}}\left(\frac{\partial \langle u_i \rangle}{\partial x_j} + \frac{\partial \langle u_j \rangle}{\partial x_i}\right) - \frac{2}{3}\delta_{ij}\frac{\partial \langle u_l \rangle}{\partial x_l}\right] - \rho g_i \tag{2}$$

Energy Equation:

$$\frac{\partial \langle \rho u_i \rangle \left(\langle E + p/\rho \rangle\right)}{\partial x_j} = \frac{\partial}{\partial x_j}\left[\lambda_{\text{eff}}\frac{\partial \langle T \rangle}{\partial x_j} + \frac{\partial \langle h_i \vec{J}_i \rangle}{\partial x_i} + \langle u_i \rangle \mu_{\text{eff}}\left(\frac{\partial \langle u_i \rangle}{\partial x_j} + \frac{\partial \langle u_j \rangle}{\partial x_i}\right) - \frac{2}{3}\delta_{ij}\frac{\partial \langle u_l \rangle}{\partial x_l}\right] + S_{\text{chem}} + S_{\text{rad}} \tag{3}$$

Species Transport Equations:

$$\frac{\partial\langle\rho u_i\rangle\langle Y_i\rangle}{\partial x_j}=\frac{\partial}{\partial x_j}\left[\left(\rho D_{i,\mathrm{m}}+\frac{\mu_\mathrm{t}}{Sc_\mathrm{t}}\right)\left(\frac{\partial\langle Y_i\rangle}{\partial x_j}+\frac{\partial\langle Y_i\rangle}{\partial x_j}\right)\right]+R_i+S_i\quad i=1,2,\ldots,N-1 \tag{4}$$

Turbulent Energy Transport Equation:

$$\frac{\partial\langle\rho u_j\rangle\langle k\rangle}{\partial x_i}=\frac{\partial}{\partial x_j}\left(\alpha_k\mu_\mathrm{eff}\frac{\partial\langle k\rangle}{\partial x_j}\right)+G_\mathrm{k}+G_\mathrm{b}-\rho\langle\varepsilon\rangle \tag{5}$$

Turbulent Dissipation Rate Equation:

$$\frac{\partial\langle\rho u_i\rangle\langle\varepsilon\rangle}{\partial x_i}=\frac{\partial}{\partial x_j}\left(\alpha_\varepsilon\mu_\mathrm{eff}\frac{\partial\langle\varepsilon\rangle}{\partial x_j}\right)+C_{1\varepsilon}\frac{\langle\varepsilon\rangle}{k}(G_\mathrm{k}+C_{3\varepsilon}G_\mathrm{b})-C_{2\varepsilon}^{*}\rho\frac{\langle\varepsilon\rangle^2}{\langle k\rangle} \tag{6}$$

where

$$\mu_\mathrm{eff}=\mu+\mu_\mathrm{t} \tag{7-1}$$

$$p_\mathrm{eff}=p+\frac{2}{3}\langle\rho k\rangle \tag{7-2}$$

$$C_{1\varepsilon}=1.42-\frac{\eta(1-\eta/\eta_0)}{1+\beta\eta^3} \tag{7-3}$$

$$C_{2\varepsilon}^{*}=C_{2\varepsilon}+\frac{C_\mu\eta^3(1-\eta/\eta_0)}{1+\beta\eta^3} \tag{7-4}$$

$$C_{3\varepsilon}=\tanh\left|\langle u_3\rangle/\sqrt{\langle u_1\rangle^2+\langle u_2\rangle^2}\right| \tag{7-5}$$

$$G_\mathrm{k}=\mu_\mathrm{t}\left[\left(\frac{\partial\langle u_i\rangle}{\partial x_j}+\frac{\partial\langle u_j\rangle}{\partial x_i}\right)-\frac{2}{3}\delta_{ij}\frac{\partial\langle u_l\rangle}{\partial x_l}\right]\frac{\partial\langle u_i\rangle}{\partial x_j} \tag{7-6}$$

$$G_\mathrm{b}=-\frac{1}{\langle T\rangle}g_i\frac{\mu_\mathrm{t}}{Pr_\mathrm{t}}\frac{\partial\langle T\rangle}{\partial x_i} \tag{7-7}$$

$$\lambda_\mathrm{eff}=\alpha C_\mathrm{p}\mu_\mathrm{eff} \tag{7-8}$$

$$\left|\frac{\alpha-1.3929}{\alpha_0-1.3929}\right|^{0.6321}\left|\frac{\alpha+2.3929}{\alpha_0+2.3929}\right|^{0.36791}=\frac{\mu_\mathrm{mol}}{\mu_\mathrm{eff}} \tag{7-9}$$

$$\alpha_0=1/Pr_\mathrm{mol}=\lambda_\mathrm{mol}/\mu_\mathrm{mol}C_\mathrm{p} \tag{7-10}$$

$$\eta=\frac{\langle k\rangle}{\langle\varepsilon\rangle}\sqrt{2S_{ij}S_{ij}} \tag{7-11}$$

$$S_{ij}=\frac{1}{2}\left(\frac{\partial\langle u_i\rangle}{\partial x_j}+\frac{\partial\langle u_j\rangle}{\partial x_i}\right) \tag{7-12}$$

The following values for the model parameters are used:

$\alpha_k=\alpha_\varepsilon=1.393;\quad Pr_t=0.9;\quad \beta=0.012;\quad g_1=g_2=0;$
$g_3=9.81\ \mathrm{m/s^2}\quad C_\mu=0.0845\quad \eta_0=4.38\quad C_{2\varepsilon}=1.68$

The generation of turbulence due to buoyancy is given by Eq. 7-7. Since a nonzero gravity field and temperature gradient are present simultaneously, the models account for the generation of k due to buoyancy (G_b in Eq. 5), and the corresponding contribution to the production of ε in Eq. 6. The degree to which ε is affected by the buoyancy is determined by the value of the constant $C_{3\varepsilon}$ (Eq. 7-5), where u_3 is the component of the flow velocity parallel to the gravitational vector and $\sqrt{\langle u_1\rangle^2+\langle u_2\rangle^2}$ is the component of the flow velocity perpendicular to the gravitational vector.

As explained by Habibi et al.,[10] the standard wall functions, based on the proposal of Launder and Spalding[17] are used.

Modeling of the combustion and turbulence/combustion interaction

Combustion is modeled by the C_1 skeletal scheme of Correa.[18] The mechanism consists of 41 reactions between 16 species (CH_4, O_2, H_2O, CO_2, CO, OH, CH_2O, H_2, HO_2, H_2O_2, O, H, HCO, CH_3, CH_3O, and N_2). Chemical reactions taking place in a turbulent flow are strongly influenced by the characteristics of turbulent regime and the turbulence/combustion interaction. The Damköhler number (Da) is the ratio of the characteristic turnover time of an eddy of the size of the turbulent integral length scale (l_t) to the characteristic transit time of the eddy through the laminar flame: $\mathrm{Da}=(l_\mathrm{t}/u')(S_\mathrm{L}/\delta_\mathrm{t})$.

Da, comparing the turbulent mixing time scale to the chemical time scale, provides insight into the flame/vortex interactions. For large Da, the chemical time scale is small compared to the eddy time scale, and turbulence is not able to affect the inner flame structure in a significant way, as the overall rate is determined by the chemical reaction rate.[5] On the other hand, low Da values imply a large chemical time scale and the flame structure is strongly modified by the turbulent eddies, as the overall rate is determined by the mixing rate. The EDC model is considered to account for turbulence/combustion interaction.[9] In this model, molecular mixing and reactions take place in concentrated isolated regions that occupy a small fraction of the total fluid volume. These regions are occupied by fine structures, whose dimensions are in the order of the Kolmogorov microscale. In EDC model it is assumed that reactions take place in the fine structures, and fine structures are modeled as perfectly stirred reactors exchanging mass and energy with the surrounding inert fluid.[5] In order to be able to treat the reactions, it is necessary to know the reacting volume fraction and the mass transfer rate between the fine structures and the surrounding fluid. These quantities are determined from turbulence theory. The volume fraction of the fine structures (that is, reacting volume) is modeled by Gran and Magnussen[19]:

$$\xi^{*3}=\left(C_\xi\left(\frac{v\varepsilon}{k^2}\right)^{0.25}\right)^3 \tag{8}$$

where * refers to fine-structure quantities, C_ξ the volume fraction constant set to 2.1377, and v is the kinematic viscosity. Species are assumed to react in the fine structures over a time scale:

$$\tau^{*}=C_\tau\left(\frac{v}{\varepsilon}\right)^{0.5} \tag{9}$$

where C_τ is the time scale constant set to 0.4082. The net reaction rate R_i for the chemical species i is computed as the sum of the rates of the N_R reactions in which the species participates:

$$R_i = M_{w,i} \sum_{r=1}^{N_R} \Gamma (\nu''_{i,r} - \nu'_{i,r}) \left(k_{f,r} \prod_{j=1}^{N_r} [C_{j,r}]^{\eta'_{j,r}} - k_{b,r} \prod_{j=1}^{N_r} [C_{j,r}]^{\eta''_{j,r}} \right) \tag{10}$$

where $M_{w,i}$ is the molecular weight of species i, Γ represents the net effect of third bodies on the reaction rate, and the expression in between brackets is the molar rate of formation/consumption of species i in reaction r. Reactions proceed over the time scale τ^* and the source term in the species transport equation (Eq. 4) for the mean species i is modeled as

$$R_i = \frac{\rho (\xi^*)^2}{\tau^* \left[1 - (\xi^*)^3 \right]} (Y_i^* - Y_i) \tag{11}$$

where Y_i^* is the fine-structure species mass fraction. The governing set of species transport equations is stiff and its numerical integration is computationally expensive. The in situ adaptive tabulation technique[20] is used to accelerate the chemistry calculations, leading to a substantial reduction in run-time.

Radiation modeling

For nonluminous flames, scattering effects need not be accounted for. The RTE at position $\vec{r}$ in direction $\vec{s}$ is given by Modest[13]:

$$\frac{dI(\vec{r},\vec{s})}{ds} + \kappa I(\vec{r},\vec{s}) = \kappa n^2 \frac{\sigma T^4}{\pi}. \tag{12}$$

A semitransparent medium is considered and the refractive index is equal to unity. Habibi et al.[10] demonstrated that the P-1 and the DOM method are suitable to solve Eq. 12. These methods are very briefly described here.

P-1 Model: The P-1 model is the simplest formulation of the more general P-N radiation model. It is derived from the expansion of the radiation intensity I into an orthogonal series of spherical harmonics.[11,12] Using only four terms, the following relation is obtained for the radiation flux:

$$\vec{q}_r = -\frac{1}{3\kappa} \nabla G \tag{13}$$

where G is the incident radiation. The problem is considerably simplified, since it is only necessary to determine a solution for G rather than for the intensity which is directional-dependent. The following expression for $-\nabla \cdot q_r$ can be directly substituted into the energy equation to account for heat sources (or sinks) due to radiation:

$$-\nabla \cdot q_r = \kappa G - 4\kappa\sigma T^4 \tag{14}$$

In the P-1 model, a transport equation for G is solved, which is elliptic in nature. As such, it requires a single boundary condition, specified for the entire enclosure surface. Once the incident radiation has been determined, the radiative heat flux is found from Eq. 14.

Discrete Ordinates Model: Conceptually, with the DOM, the RTE is solved for a set of n different directions, $\vec{s}_i$, $i=1, 2, \ldots, n$, and the integrals over these directions are replaced by numerical quadratures. In order to ensure conservation of radiative energy, the fully finite volume approach is followed in space as well as in direction.[10] This method uses an exact integration to evaluate the solid angle integrals. The RTE is solved for a finite number of discrete solid angles, each associated with a vector direction $\vec{s}$ fixed in the global Cartesian system (x, y, z). Furthermore, Eq. 12 for the RTE is transformed into a transport equation for radiation intensity in the spatial coordinates (x, y, z).

$$\nabla \cdot (I(\vec{r},\vec{s})\vec{s}) + \kappa I(\vec{r},\vec{s}) = \kappa n^2 \frac{\sigma T^4}{\pi} \tag{15}$$

Radiative properties modeling

The combustion products, CO, CO_2, and H_2O and in a lesser amount the fuel component CH_4, are strongly selective absorbers and emitters. As in the previous work,[10] the weighted sum of gray gases model (WSGGM)[21] is used to compute the absorption (or emission) coefficient of the mixture of gases. In this method the nongray gas is replaced by a number of gray gases, for which the heat transfer rates are calculated independently. The total heat flux is finally calculated by adding up the heat fluxes of the gray gases, taking into account certain weight factors.

The basic assumption of the WSGGM is that the total emissivity over the distance s can be presented as

$$\varepsilon = \sum_{i=0}^{I} a_{\varepsilon,i}(T)[1 - e^{-\kappa_i p s}] \tag{16}$$

where $a_{\varepsilon,i}$ is the emissivity weighting factor for the ith gray gas, the bracketed quantity is the ith gray gas emissivity, κ_i is the absorption coefficient of the ith gray gas, p is the sum of the partial pressures of all absorbing gases, and "s" is the path length. Since, for an infinitely thick medium, the absorptivity approaches unity, it is found that $\sum_{i=0}^{I} a_{\varepsilon,i}(T) = 1$. Still, for a pure molecular gas with its "spectral windows" it would take very large path lengths, indeed, for the absorptivity to be close to unity. For this reason the summation starts with $i = 0$ (with an implied $a_{\varepsilon,0} = 0$), to allow for spectral windows. The absorption coefficients κ_i are taken from Smith et al.[22] and the temperature dependence of $a_{\varepsilon,i}$ is approximated by $a_{\varepsilon,i} = \sum_{j=1}^{J} b_{\varepsilon,i,j} T^{j-1}$.

NO_x modeling

The transport equations for NO, HCN, and N_2O are solved, taking into account convection, diffusion, production, and consumption of the relevant species (Eq. 4). The relationships among NO_x formation rate, temperature, and species concentrations are highly nonlinear. Hence, if time-averaged compositions and temperatures are used in NO_x formation models, significant errors will result. Thus, temperature

and composition fluctuations are taken into account through the preassumed β-probability density functions (PDF).[23] A joint-variable PDF in terms of the combination of normalized temperature and CH_4 mass fraction is used to predict the NO emission.

For construction of the joint PDF's the mean values of the β-PDF distribution for temperature and CH_4 mass fraction are taken from the solution of their respective transport equations. The variance of the β-PDF distribution, σ^2, is computed from the following variance transport equation:

$$\frac{\partial \rho u_i \sigma^2}{\partial x_i} = \frac{\partial}{\partial x_j}\left(\frac{\mu_t}{\sigma_t}\frac{\partial \sigma^2}{\partial x_j}\right) + C_g \mu_t \left(\frac{\partial \bar{m}}{\partial x_j}\right)^2 - C_d \rho \frac{\varepsilon}{k}\sigma^2 \qquad (17)$$

where $\bar{m}$ stands for $\tilde{T}$ or $\tilde{Y}_{CH_4}$, as computed in the furnace simulation. The default values are used for σ_t, C_g, and C_d: 0.85, 2.86, and 2.0, respectively.

Then, the mean turbulent reaction rate $\overline{S}_{NO}$ is described in terms of the instantaneous rate S_{NO} and a joint PDF of different variables.

$$\bar{S}_{NO} = \int_{Y_{CH_4,min}}^{Y_{CH_4,max}} \int_{T_{min}}^{T_{max}} S_{NO}(T, Y_{CH_4}) P(T) P(Y_{CH_4}) dT dY_{CH_4} \qquad (18)$$

$P(T)$ and $P(Y_{CH_4})$ are the corresponding β-PDF of temperature and CH_4 mass fraction, respectively. A similar treatment is applied in the calculation of the HCN and N_2O source terms in the NO transport equations. The NO formation rate (S_{NO} in Eq. 18) is calculated from the following models.

Thermal NO Formation: Thermal NO formation is computed from the extended Zeldovich mechanism with the kinetic parameters of Hanson and Salimian.[24] The partial equilibrium approach is used to predict the OH radical concentration. The equilibrium model according to Westenberg[25] is used for the prediction of the O-atom concentration. The equilibrium assumption is justified by a reduction in the importance of radical overshoots at higher flame temperatures.[26]

Prompt NO Formation: Prompt NO formation is the most prevalent mechanism in fuel-rich flame regions. In the early stages of the flame, where prompt NO is formed, the O concentration is high and the N radical almost exclusively forms NO rather than nitrogen. The prompt NO formation rate is calculated using the model proposed by De Soete.[27]

NO Formation from Intermediate N_2O: This mechanism is important mainly at elevated pressures and oxygen-rich conditions. It may also be important in systems operated in flameless mode (e.g., diluted combustion, flameless combustion, flameless oxidation, and FLOX systems). So, it is expected that the impact of this mechanism on overall NO formation is small in this study.

NO Re-burning: The partial equilibrium approach, based on the model proposed by Kandamby et al.[28] which was developed by Pereira et al.,[29] was used. It is assumed that methane is the major reburning fuel with unity equivalence ratio. Fluctuations in CH_4 mole fraction are accounted for.

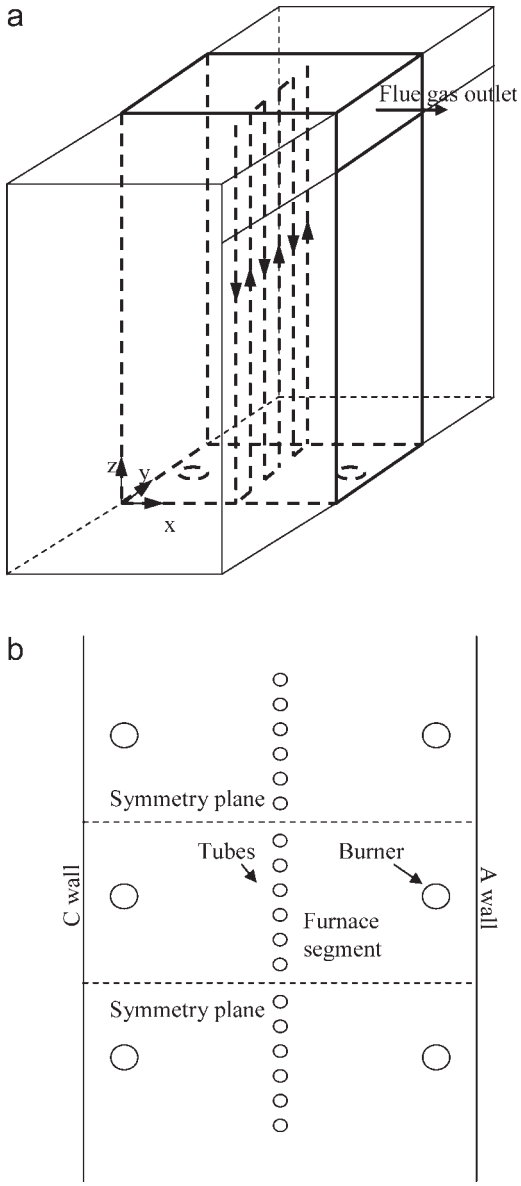

Figure 1. (a) Schematic representation of the furnace and the simulated segment; (b) top view of the simulated segment.

Simulation Set-up

Furnace geometry and operating conditions

A representative segment of an industrial scale steam cracking furnace is simulated. The segment contains two flame burners that are positioned on the left and the right side of six reactor tubes. Fuel (CH_4/H_2) and air are premixed before entering the radiation section. The mixture composition is 94.3% CH_4 and 5.7% H_2 by mass. A schematic representation of the simulated furnace segment and its top view are shown in Figures 1a,b. The basic geometries of the furnace and reactor coils and the firing conditions are given in Table 1.

Since the tube coils have a hexagonal cross section, a tetrahedral/hybrid structured grid that provides satisfactory geometrical flexibility and reliable results[3] was used. The com-

Table 1. Furnace Dimension and Operating Conditions

Furnace segment	
Height (*Z*-direction), m	6.796
Length (*Y*-direction), m	1.2
Width (*X*-direction), m	3.0
Thickness of refractory, m	0.23
Thickness of insulation, m	0.05
Outlet starts height, m	0.536
Number of burners	2
Burner diameter, m	0.23
Reactor coils*,†	
Number of reactor tubes	6
Total reactor length (six tubes), m	38.68
External tube diameter, m	0.12
Internal tube diameter, m	0.10
Firing condition	
Fuel gas flow rate, kg/s	0.4226
Fuel equivalence ratio	0.94
Fuel composition, wt %	
CH_4	94.3
H_2	5.7
Material properties	
Emissivity of the furnace wall (−)	0.85
Emissivity of tube skin (−)	0.6
Thermal conductivity of refractory, W/(m K^{-1})	0.394
Thermal conductivity of insulation, W/(m K^{-1})	0.19
Thermal conductivity of tube skin, W/(m K^{-1})	$-8.432 + 3.04 \times 10^{-2}$ T

*Center points of the six cylindrical tubes are located at $X = 1.5$ m and ($Y = 0.1$, 0.3, 0.5, 0.7, 0.9, and 1.1 m).
†All tubes start from $Z = 0.2$ m and end at $Z = 6.646$ m height.

putational domain is virtually discriminated into separate blocks: one volume-centered around the tube coil with dimension $40 \times 120 \times 679.6$ cm^3, two volume-centered above the left and right hand burners with dimension $40 \times 40 \times 300$ cm^3, and two adjacent volumes near the refractory walls with dimension $15 \times 120 \times 679.6$ cm^3. Some features of the meshing scheme are presented in Table 2. Solution-adaptive grid refinement is performed to efficiently reduce the numerical error in the solution, as described by Habibi et al.[10] The operating pressure is set to 101,325Pa.

For the DOM radiation model, each octant of the angular space 4π at any spatial location is discretized into ($N_\theta = 8$) $\times$ ($N_\phi = 8$) solid angles. Therefore for 3D calculations, a total of $8 \times 8 \times 8$ directions are solved. Essentially, control angles can straddle the control volume faces, so that they are partially incoming and partially outgoing to the face. Since control volume faces do not in general align with the global angular discretization, the problem of control angle overhang[30] arises.

Table 2. Some Aspects of the Meshing Scheme

	3-D Tetrahedral Cells	2-D Triangular Elements		Nodes
		Wall Faces	Interior Faces	
Number	65,594	20,378	120,999	15,867
Memory usage, MB	11	10		1
Worst elements				
Equiangle skewness	0.76	0.69		
Equisize skewness	0.77	0.74		
Aspect ratio	4.24	2.67		

This problem is overcome using pixelation. In this work, each overhanging control angle is divided into 3×3 pixels.

Boundary conditions

As mentioned, the standard wall functions are used for the wall boundary conditions. At the burner inlets, the velocity, temperature, and mixture composition are imposed. At the furnace exit, the outlet pressure is imposed. In order to meet the desired mass flow rate, a method based on Bernoulli's equation ($dp = 0.5\ \rho_{ave}\ (\dot{m}^2 - \dot{m}_{req}^2)/(\rho_{ave}A)^2$) is applied for adjusting the pressure in a pressure-outlet zone. dp is the change in pressure, $\dot{m}$ is the current computed mass flow rate at the pressure-outlet boundary, $\dot{m}_{req}$ is the required mass flow rate, ρ_{ave} is the computed average density at the pressure-outlet boundary, and A is the area of the pressure-outlet boundary. This pressure adjustment approach is very efficient. The results of induced error calculation in the mass balance for different code implementations are shown in Table 3. The possibility of the reverse flow at the outlet boundary, during the solution process is taken into account. A zero flux of all quantities is assumed across the symmetry boundaries. As the shear stress is considered zero at these boundaries, they can also be interpreted as a "slip" wall in viscous-flow calculations. The heat loss from the furnace refractory walls is set equal to 3% of the furnace fired duty. A linearly increasing process gas temperature profile, taken from Stefanidis et al.,[5] is applied as boundary condition for the tube-sides in our simulations. Zero mass flux is imposed for all species.

For the P-1 radiation model, the boundary condition for the incident radiation equation is obtained from the dot product of the outward normal vector $\vec{n}$ and Eq. 15. For diffuse gray walls it leads to

$$q_{out} = -\frac{\varepsilon_w}{2(2-\varepsilon_w)}(4\sigma T_w^4 - G_w) \tag{19}$$

For the DOM radiation model, the furnace wall surface temperature is calculated from the following equation, while imposing q_{out}:

$$q_{out} = (1-\varepsilon_w)q_{in} + n^2\varepsilon_w\sigma T_w^4 \tag{20}$$

where

$$q_{in} = \int_{\vec{s}.\vec{n}>0}^{4\pi} I_{in}\vec{s}.\vec{n}\, d\Omega \tag{21}$$

Table 3. Some Aspects of Simulation Results with Different Radiation Models

	% Error in Mass Balance	Max. Predicted Temperature, K	% Error in Heat Balance	% Thermal Efficiency
No-radiation	1.617 E −05	2234	0.103	32.3
P-1	0.016	2134	0.264	43.6
DOM	0.009	2134	0.003	43.9

I_{in} is the intensity of the incoming radiative beam, Ω is the hemispherical solid angle, and $\vec{n}$ is the normal pointing out of the domain. For both radiation models, the internal emissivity at the burner inlets and outlets is set equal to one. The external black body temperature for the burner inlet and the furnace exit are set to 343 and 1500 K, respectively.

Solution procedure

The governing equations for the conservation of mass, momentum, energy, turbulence, chemical species, and radiation are solved sequentially (i.e., segregated from one another) with Fluent, version 6.2.[31] The NO_x equations are solved in a postprocessing step. As combustion reactions lead to a large heat release, subsequent density changes and large accelerations in the flow, it is difficult to obtain a converged solution for a number of reasons. First, the impact of the combustion reactions on the basic flow pattern is strong, resulting in a strong coupling between the mass/momentum balances and the species transport equations. To reach a stable converged solution under these conditions, a two-step solution procedure is used. In the first step, the flow, energy, and species equations are solved with reactions "disabled" (the "cold-flow", or unreacting flow). When the basic flow pattern has thus been established, the reactions are "enabled" and the calculation is continued. To minimize the numerical error, no separate transport equation for the N_2 species concentration is solved. Instead, the N_2 concentration is determined from normality conditions. The discontinuities in the nodal points which arise from the structured meshing scheme are captured by construction of a sophisticated interpolating surface.

A control-volume-based method is used. Central differencing (second order) is applied for pressure and viscous terms. The convective terms in the nonlinear governing equations are discretized by a second-order upwind scheme and linearized to give a set of equations for the dependent variables in every computational cell. The resultant linear system with a sparse coefficient matrix is then solved to yield an updated flow-field solution. Since high values for pressure-correction under relaxation lead to instability problems, the SIMPLE algorithm[32] with a slightly more conservative under-relaxation value (up to 0.7) is used. To alleviate the instabilities in solution, a lower under-relaxation factor for density, equal to 0.5, is used.

The code uses a point implicit (Gauss-Seidel) linear equation solver in combination with an algebraic multigrid method to solve the resultant set of equations in each cell. Since the velocities obtained in this step may not satisfy the continuity equation locally, a pressure correction equation is then solved to obtain the necessary corrections for the pressure and velocity fields, as well as for the face mass fluxes, such that the continuity is satisfied. Next, the equations for turbulence, energy, species mass fraction, and radiation are solved using the previously updated values of the other flow variables. For more details, the reader is referred to the Fluent manual.[31]

The calculations are started with small (conservative) under-relaxation parameters, and these are increased gradually as the iterations proceed and the solution begins to settle down. A residual for the density-based solver is simply the time rate of change of the conserved variable. To judge convergence by examining the residuals, the scaling with respect to the largest absolute value of the residual in the first five iterations is employed. The convergence criterion is set to 10^{-6} for all governing equations, except for the continuity equation that is set to 10^{-4}. The scaled residuals of an equation at each iteration are compared with the corresponding convergence criteria. If it is less than this specified value, the equation is converged for that time step.

A grid sensitivity study has been performed. Since testing for mesh-independence by uniformly refining the entire mesh is computationally expensive, adaptation can often be much more efficient in that only selected regions of the flow-field are refined. As already mentioned, solution-adaptive grid refinement is performed to efficiently reduce the numerical error in the solution. After each adaptation step, all mesh modification strategies, i.e. skewness improvement, edge swapping, and node movement are applied. Grid independence is achieved when further mesh refinement do not yield a significant change in the the calculated velocity, temperature, and species mass fraction fields.

Results and Discussion

Turbulence regime

Table 4 provides an indication of different turbulent characteristics for the turbulent premixed combustion regime. These values are calculated based on the conditions of fresh, unburned fuel/air mixture at the burner inlet. The turbulent Reynolds number, $Re_t = u' l_t / \nu$ is determined based on the assumption of $l_t = 0.1 d_o$, where d_o is the jet burner diameter. It is assumed that the turbulence intensity is equal to 10% of the jet velocity magnitude at the burner inlet. Combustion is clearly turbulent. For the determination of Da, the mixing time (that is, turbulent time scale) is calculated as l_t/u' and the chemical time scale is calculated as α/S_L, where α is the thermal diffusivity and S_L is the laminar burning velocity, calculated using equations given by Byggstøyl and Magnussen.[33] The kinematic viscosity, ν and the thermal diffusivity, α, are determined for the fresh unburnt mixture at fuel inlet temperature and furnace pressure. Since Da is large, turbulence is not able to affect the inner flame structure, which thus remains close to a laminar flame, wrinkled by turbulent motions (flamelet limit). Under these conditions, the mean burning rate can be estimated from the burning rate of a laminar flame multiplied by the overall flame surface. Since $u'/S_L > 1$, the turbulent motion leads to flame front interaction, with the formation of pockets of fresh and burnt gases. This regime is identified as the "thin flame regime with pockets" or "corrugated flamelet regime."

Table 4. Turbulent Characteristics of the Flow Inside the Furnace

Turbulent length scale (l_t), m	0.023
Velocity fluctuations (u'), m/s	0.65
Turbulent Reynolds number (Re_t)	397
Turbulent time scale (τ_{mix}), s	0.036
Chemical time scale (τ_{chem}), s	0.00037
Damköhler number (Da)	98
Laminar flame speed (S_L), m/s	0.34

Table 5. Mass Average Relevant Quantities of Fine Structures

	Fine Structures Temperature, K	Fine Structure Mass Transfer Rate, s^{-1}	Fine Structure Volume Fraction	Fine Structure Time Scale, s
Adiabatic	2207	272	0.54	0.036
P-1	1267	227	0.59	0.050
DOM	1294	268	0.56	0.041

The average time scale of the fine structures and the mass transfer rate per unit of fluid between the fine structures and the surrounding fluid is presented in Table 5. Figure 2 shows that the fine structures, which are responsible for the main part of the energy dissipation, are localized in the highly strained regions. The rate of molecular mixing is determined by the rate of mass transfer between the fine structures and the surrounding fluid. Since it is assumed that the various species mix homogeneously within the fine structures, the mean transfer rate of a given species, from the surrounding fluid into the fine structures, equals the mean consumption rate of the same species within the fine structures.

Thermal quantities

Figure 3 shows the temperature contours of each radiation model in the vertical cross section of the furnace at $Y = 0.6$ m, through the center of the burners. The results of the two radiation models are compared with the relevant contour of adiabatic simulation. Note the differences in the maximum temperature values. A clear flame structure is obtained with both radiation models. The predicted temperature field in the adiabatic simulation is unrealistic, with excessive temperatures.

An impression of the flow field pattern is shown as velocity vectors at $Y = 0.6$ m in Figure 4 (results obtained with DOM; P-1 results are very similar, not shown). Two jets are observed above the burners, with a strong increase in velocity in the flame region due to the temperature rise (expansion effect). Two large recirculation zones are predicted in the upper left part and the lower core of the furnace. The upper recirculation zone starts approximately from 3.5 m height and extends to the upper wall of the furnace. This recirculation zone is due to the asymmetric outlet of the flue gas in the furnace and is an obstruction for the flue gas flow. The lower core recirculation zone starts at the bottom of the furnace in between the burner cups and extends to approximately $Z = 4.0$ m height, with the strongest effect near the right-side burner.

Figures 5 and 6 provide vertical and horizontal temperature profiles in the same vertical cross section (i.e. $Y = 0.6$ m). The vertical temperature profiles are those calculated along the centerline of the left hand side burner. The predictions of DOM and P-1 model are close to each other. The maximum predicted temperatures are obtained at a height of about $Z = 0.5$ m. The temperature profiles show that the combustion took place near the burners, with high temperatures close to the burner cup. The increase in temperature is closer to the burner than with the EBU model and simplified reaction kinetics.[10] The temperature profile for the adiabatic model increases monotonically up to $Z = 0.5$ m and then flattens asymptotically up to the furnace ceiling. Beyond the flame zone ($Z > 0.5$ m), the difference between this model and the radiation models increases considerably with furnace height. Between 0.5 and 3.5 m height, the temperature profiles calculated with the DOM and the P-1 model differ slightly from each other. Slightly higher temperatures are predicted with the DOM.

In the horizontal temperature profiles at a height of 0.5 m (see Figure 6a), clear differences are seen between the adiabatic simulation and the simulations with two radiation models. In the latter, the highest temperatures are observed locally above the two burners, showing the flame structure. This is a significant difference with the results of the previous work,[10] where the EBU model is applied with simplified chemical kinetics. Under these conditions, ignition has not yet occurred at a height of 0.5 m. Unfortunately, the absence of experimental data does not allow validation of the model performance. A heat sink region is observed around the reactor tubes, because of the heat flux toward the tubes (see later). In line with the results of Figure 5, there is no significant difference in peak temperatures between the DOM and the P-1 radiation model. At a height of 1.5 m (Figure 6b), the situation remains similar. The temperature profiles at 3.5 m (Figure 6c) and 5.5 m (Figure 6d) are outside of the flame zone and only flue gas is present. Around the reactor tubes, the local heat sink is still clearly seen: the heat sink extends over the entire furnace height. As explained by Habibi et al.,[10] the temperature profiles at a height of 5.5 m show some asymmetry because the furnace exit is situated at one side of the furnace. As discussed in Figure 4 the flow field is asymmetric as well, with the flue gas velocities being higher at the side of the furnace exit, resulting in more convection of hot gases and higher mean temperatures.

Figure 7 shows the refractory furnace wall temperature profiles at $Y = 0.6$ m on the front and back wall of the furnace calculated with the P-1 model and the DOM. The comparison shows a globally higher temperature prediction with DOM than with P-1. The asymmetry in the furnace outlet,

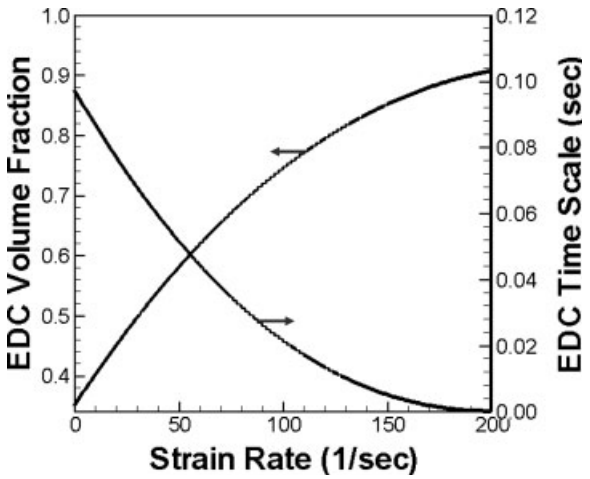

Figure 2. Vertical profiles of the fine structure volume fraction (left) and time scale (right) versus strain rate above the left hand side burner.

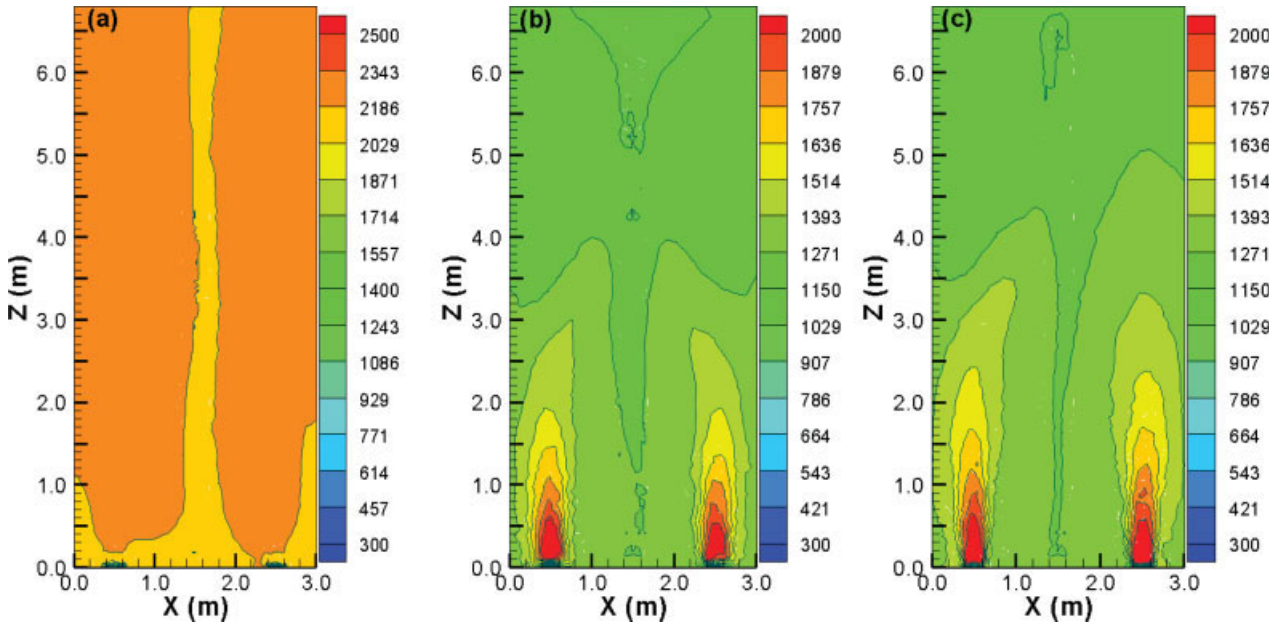

Figure 3. Static temperature profiles at $Y = 0.6$ m. (a) Adiabatic, (b) P-1 model, (c) DOM.

[Color figure can be viewed in the online issue, which is available at www.interscience.wiley.com.]

affecting the flow field as reported earlier, is also seen in the temperature difference between the front and the back wall of the furnace.

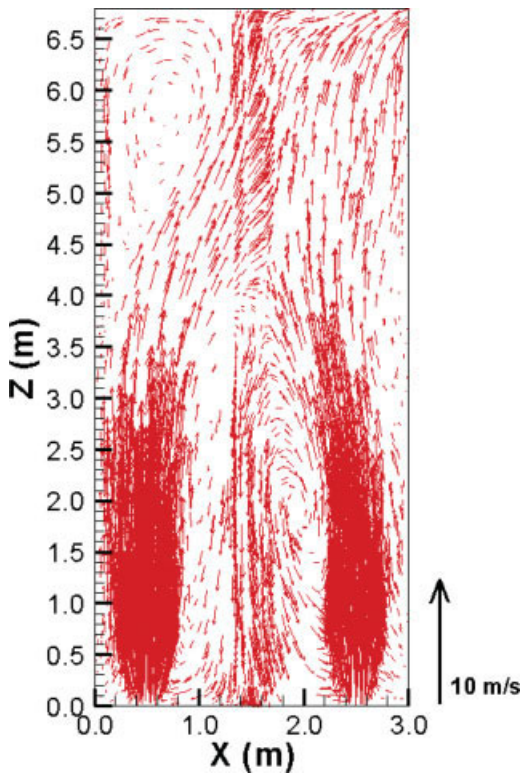

Figure 4. Velocity vectors at $Y = 0.6$ m (DOM).

[Color figure can be viewed in the online issue, which is available at www.interscience.wiley.com.]

Combining Figures 5 and 7, three regions can be distinguished based on the temperature profiles, namely preheating, combustion, and postcombustion. In the (very small) preheat region, the wall temperature is significantly higher than the gas temperature, and energy is transferred from the wall to the gas. Once the fuel gas reaches the ignition temperature, the fuel mixture burns rapidly, releasing heat and causing a sharp rise in the gas temperature in the combustion region. The combustion region is relatively narrow (or localized), a characteristic of highly activated reactions. Even at these relatively small scales, diffusion of heat within the gas and radiation are low compared to the rate of heat release.

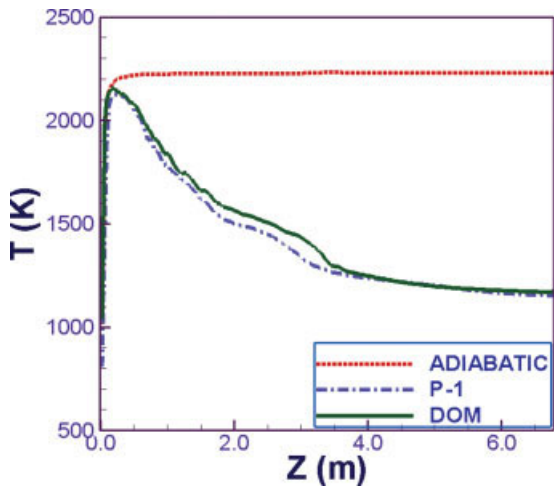

Figure 5. Evolution of the gas temperature at $Y = 0.6$ m above the left hand side burner.

[Color figure can be viewed in the online issue, which is available at www.interscience.wiley.com.]

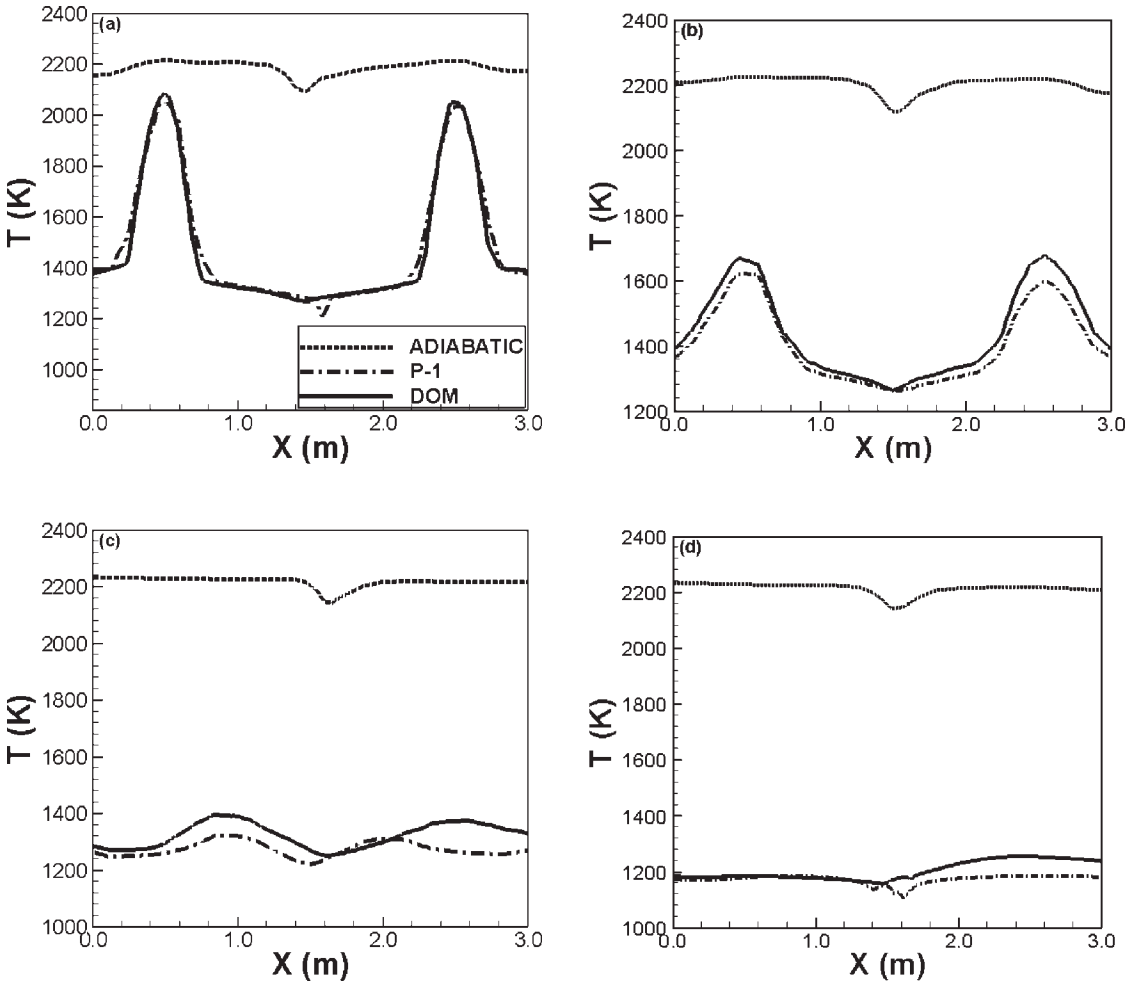

Figure 6. Evolution of the temperature at different height of the furnace at $Y = 0.6$ m. (a) $Z = 0.5$ m, (b) $Z = 1.5$ m, (c) $Z = 3.5$ m, (d) $Z = 5.5$ m.

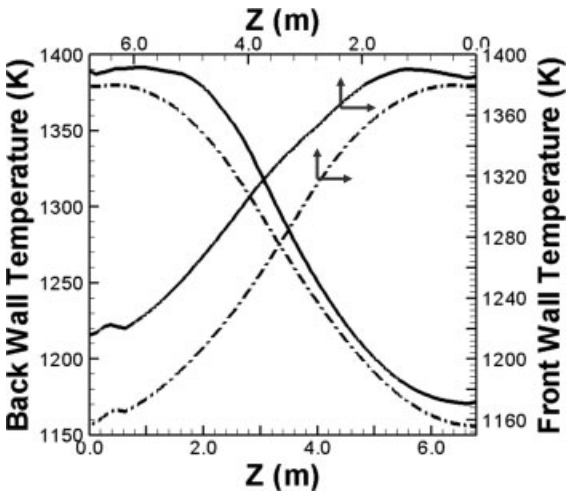

Figure 7. Predicted refractory temperature profiles at $Y = 0.6$ m for the front ($X = 3.0$ m) and back ($X = 0.0$ m) furnace walls with DOM (solid line) and P-1 (dashed line).

As a result, the gas centerline temperature in this region approaches the adiabatic flame temperature. In the postcombustion region, after the reactants have been consumed, the reaction stops and the flue gas cools down, transferring heat to the furnace walls and reactor tubes. There are no significant axial or transverse gradients within this region.

The fire-side tube skin temperatures are not known a priori. Assuming that the fireside convection coefficient (computed by the model), the incident radiative flux, the emissivity, and conductivity of the tube material and the process and flue gas temperature profiles are known, the inner and outer tube skin temperatures are calculated by constructing an energy balance over the tube wall. The predicted average fire-side tube skin temperature for each tube along with the imposed process gas temperature inside the cracking tubes is shown in Figure 8a. Large differences are observed between the predicted tube skin temperature in the adiabatic simulation, and the temperature where radiation is accounted for. The predicted tube skin temperature increases gradually from the first tube toward the sixth tube.

The results in terms of total heat duty of the tubes are shown in Figure 8b, accounting that radiation has a profound effect on the predicted heat flux (increasing by a factor of 7).

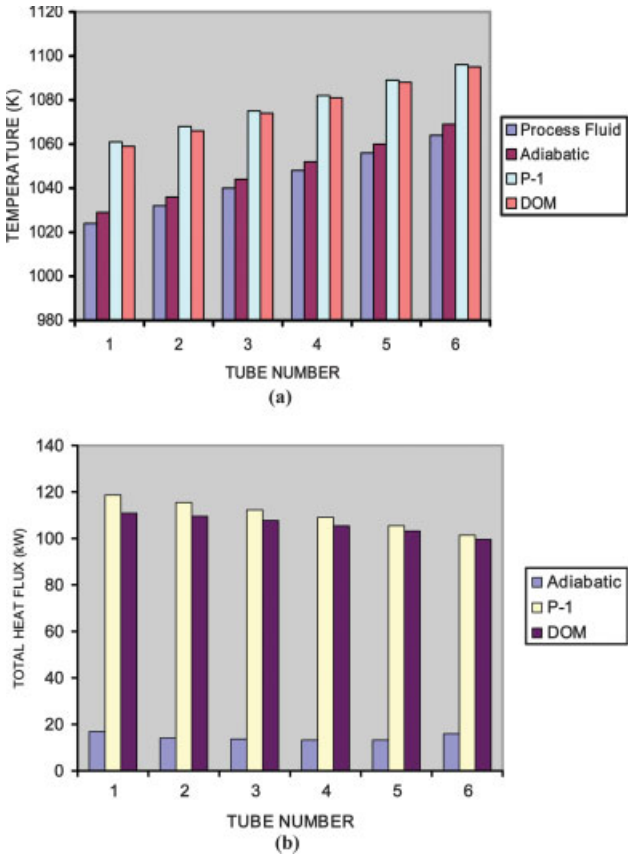

Figure 8. Predicted average fire-side tube skin temperature and total heat flux for each cracking tube.

[Color figure can be viewed in the online issue, which is available at www.interscience.wiley.com.]

This illustrates that radiative heat transfer strongly dominates convective heat transfer. The predicted heat duty with the adiabatic model is unrealistic, considering that the inner tubes absorb less thermal energy than the outer tubes. As the driving force for heat transfer gradually decreases from tube-1 to tube-6, because of the higher process gas temperature, a decreasing trend in the heat flux is observed with the DOM and P-1 model.

The superficial radiative heat flux is computed for each cracking tube. The radiation heat flux varies between 20 and 59 kW/m^2, with the highest values near the flame zone and the lowest value in the top of the furnace. The overall trends for all tubes are the same and are not shown here for the sake of brevity.

The maximum incident radiation on the furnace front and back wall corresponds to the projection of the flame on the wall (not shown).

Figure 9 shows the contour plots of the emission, the absorption, and the radiative source term in the energy equation, with DOM in the plane $Y = 0.6$ m. In the entrance zone of the furnace, there is a limited self-absorption, and the net radiative source term is positive. As a result, the inclusion of radiation slightly increases the gas temperature. In the flame zone, emission dominates absorption, and inclusion of radiation leads to a net temperature decrease. In the postflame zone, above $Z = 3.8$ m, the absorption and emission terms are of the same order of magnitude.

When the axial profiles of emission, absorption, and net radiative heat loss above a burner are compared quantitatively, a sharp increase in both emission and absorption of the same order of magnitude is observed at the start of the postflame zone. The postflame zone is calculated slightly closer to the burner with the P-1 model than with the DOM (not shown).

Species quantities

Species concentration profiles in the furnace suggest the presence of two regions: (i) a highly nonequilibrium reaction zone (a turbulent premixed flame anchored at the inlet jet) and (ii) a postflame region. Figure 10 shows nine equidistant contours of CH_4 and H_2 mass fraction at $Y = 0.6$ m. The contour values are normalized with respect to the values at the burner inlets. In line with the temperature profiles, it is clear that the combustion zone is confined to a region above the burner inlets. Similar results are obtained for the major combustion products CO_2 and H_2O (not shown).

The results for CO, an intermediate combustion product, are presented in Figure 11. The conversion from CO to CO_2 proceeds faster in the adiabatic simulations, because of the higher gas temperatures.

Taking into account convection, diffusion, formation, and consumption, the species transport equations for NO, HCN, and N_2O are solved. The equilibrium values for temperature, stable species, O atoms, and OH radicals are assumed. Figure 12 compares the rate of thermal NO formation (a), prompt NO formation (b), NO formation from the N_2O intermediate mechanism (c), and the rate of overall NO formation (d), calculated with the DOM model at $Y = 0.6$ m. The contours calculated when using the adiabatic model and the P-1 model are not shown for the sake of brevity. The thermal NO formation rates in the adiabatic simulation are higher due to higher temperature predictions. Some differences between the P-1 model and the DOM are calculated: the DOM contours are slightly narrower and longer. The prompt NO formation rates for the different models are all in the same order of magnitude, irrespective of the predicted temperature field, and about 10^{10} times smaller than the thermal NO formation rates. NO formation from molecular nitrogen (N_2) via nitrous oxide (N_2O) also comprises a small part of the total NO formation. Considering all NO formation models results in the prediction of the overall NO formation rate. The NO formation is concentrated in the region of the strongly nonequilibrated combustion chemistry. The individually determined thermal and prompt NO_x mass fractions do not add up to the levels predicted when the two models are combined. This is because reversible reactions are involved. NO_x produced in one reaction can be destroyed in another reaction.[31]

Inclusion of the reburning model does not considerably affect the overall NO formation rate in the simulation cases. The rate of reburning is calculated to be about 10^{-6} to 10^{-4} times the thermal NO_x production rate.

The mass (in ppm) of total NO species in the reaction volume is shown at $Y = 0.6$ m in Figure 13. The peak concentration of NO is located in a region of high temperature

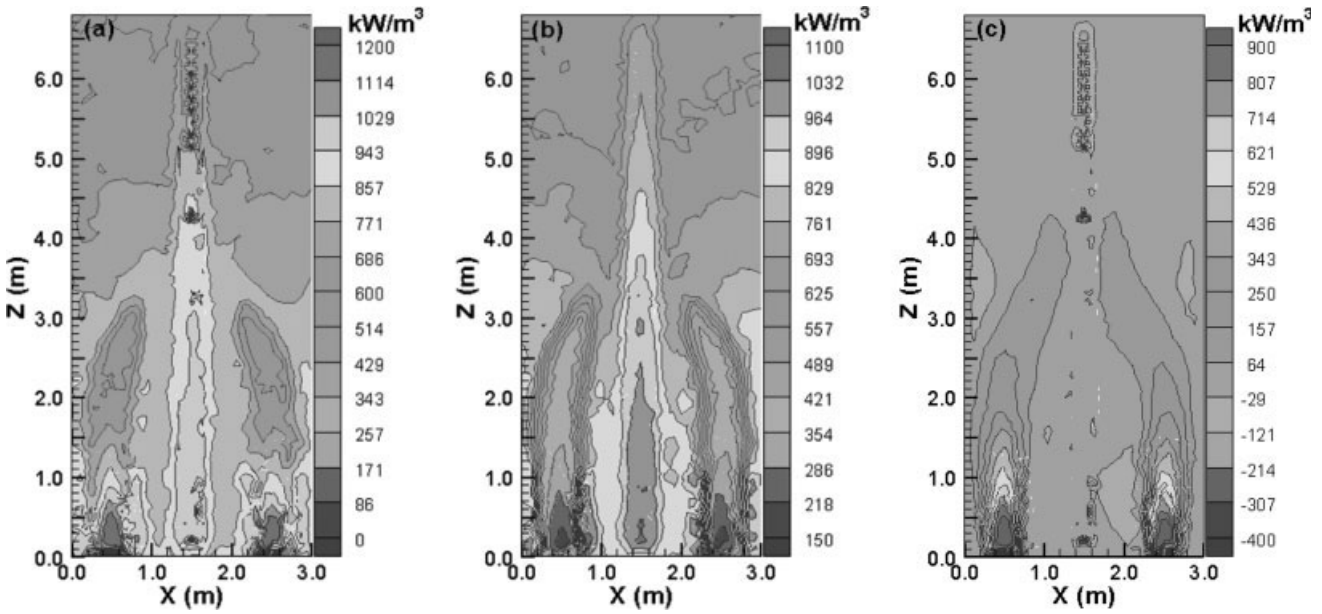

Figure 9. The predicted (a) emission term, (b) absorption term, and (c) radiative source terms, $-\nabla \cdot q_r$ with DOM ($Y = 0.6$ m).

where oxygen and nitrogen are available. This picture differs strongly from Figure 10, because of the very slow time scale of NO_x chemistry. Typically, the combustion and turbulence time scales are in the order of 1 s, while the time scales of NO reactions are in the order of 3.5×10^6 s. Thus, turbulence can strongly affect the NO concentration field (through

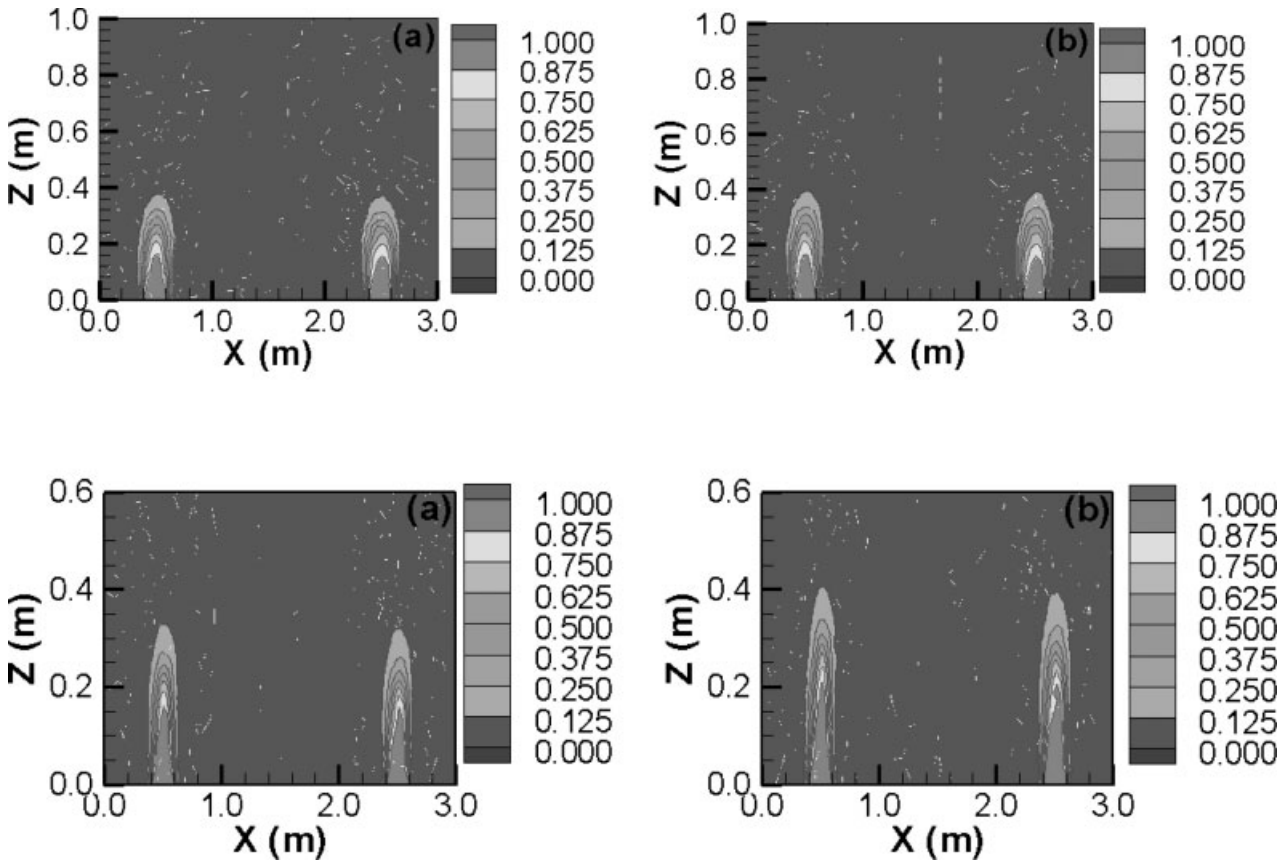

Figure 10. Normalized mass fraction of CH_4 (top) and H_2 (bottom) at $Y = 0.6$ m. (a) Adiabatic and (b) DOM.

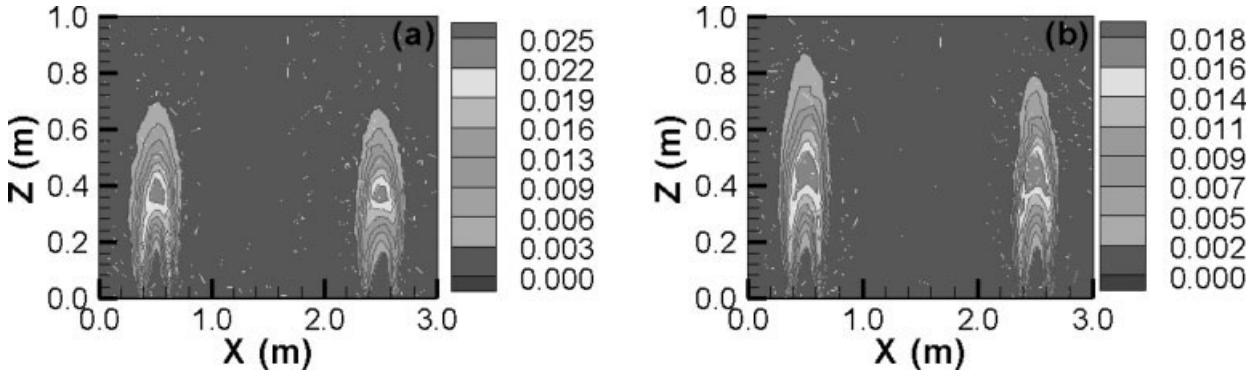

Figure 11. Normalized mass fraction of CO at $Y = 0.6$ m. (a) Adiabatic and (b) DOM.

convection and diffusion), and the NO mass fraction contours do not resemble the NO formation field contours. Finally, it is remarked that the average NO mass fraction at the furnace exit is about 0.0036 for adiabatic model, 0.00064 for P-1 model, and 0.00078 for DOM. Clearly, inclusion of radiation considerably affects the amount of NO produced in the furnace. Furthermore, no significant changes are observed for the NO mass fraction in the upper part of the furnace ($Z = 3.0$ m).

Conclusions

A 3D numerical simulation has been presented for a gas-fired steam cracking furnace. The RNG k-ε turbulence model is applied, in combination with the EDC model and a C_1-skeletal combustion mechanism. The results of adiabatic simulation case and two simulation cases with the P-1 radiation model and the DOM are compared. The major conclusions are

- The combustion regime in the furnace is the "corrugated flamelet regime";
- The results with the DOM and P-1 model are very similar. This is found for the gas temperatures, wall temperatures, heat fluxes toward the reactor tubes, as well as for chemistry calculation results (species profiles and production or consumption rates). P-1 calculations require less CPU-time, but DOM has a broader application range, so that in general probably the DOM model is to be preferred;
- Ignition takes place closer to the burner when the EDC model is used for turbulence/chemistry calculation as com-

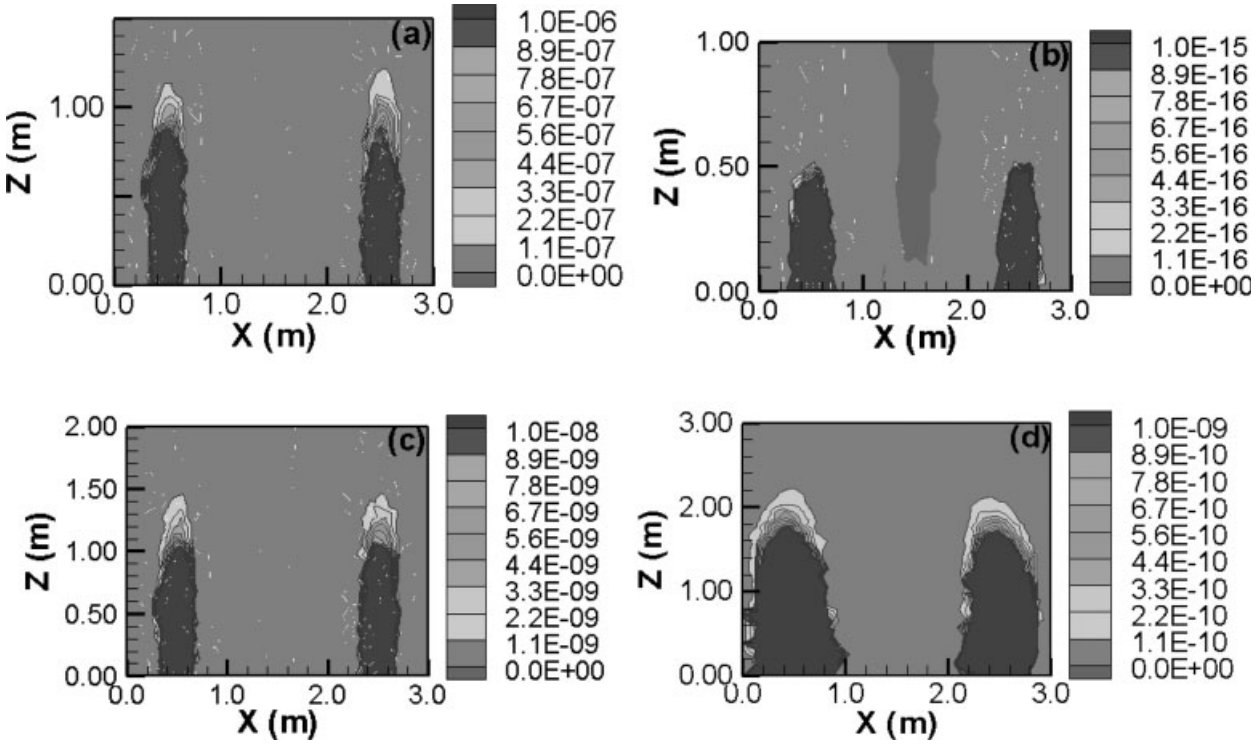

Figure 12. Rate of NO formation with DOM [kg/(mol m^3)] at $Y = 0.6$ m. (a) Thermal, (b) prompt, (c) N_2O intermediate mechanism, and (d) overall.

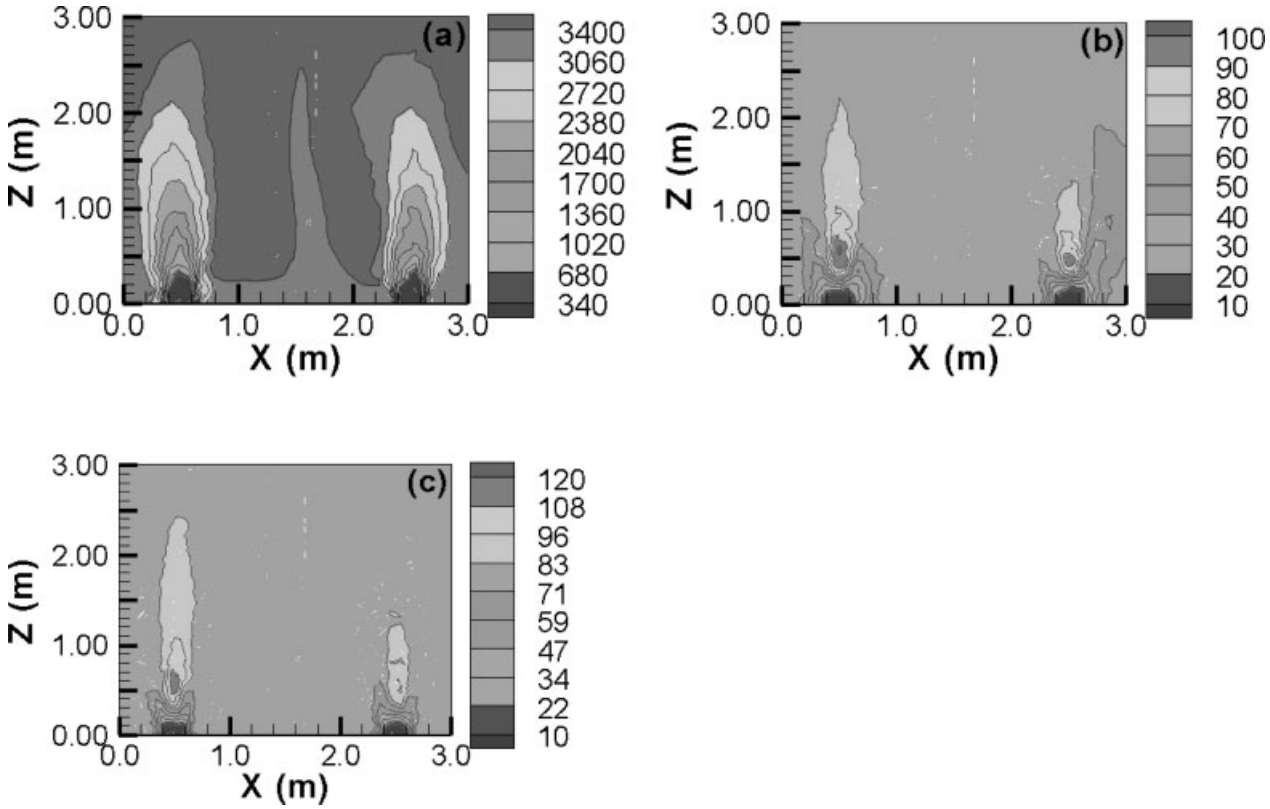

Figure 13. Mass (in ppm) of NO at $Y = 0.6$ m. (a) Adiabatic, (b) P-1, and (c) DOM.

pared to the EBU model, in combination with simplified chemical kinetics (Habibi et al.[10]);

- Three regions are distinguished: preheat region (very small), combustion region (anchored at the jet inlet), and postcombustion region, where heat is transferred from the hot flue gases toward the walls and tubes;
- Inclusion of radiation is crucial for the correct determination of the heat flux toward the tubes; radiation strongly dominates over convection;
- The asymmetry in the flow field due to the asymmetric furnace outlet is also found in gas and furnace wall temperature profiles;
- Thermal NO formation is by far the most important mechanism in the NO_x chemistry. Combination with prompt NO formation is not straightforward, because of interaction between the two mechanisms. The reburning mechanism is not significant for this combustion system.

As a closing remark we note that the results presented here, obtained with Fluent, are in line with what is reported by Stefanidis et al.[5] and Habibi et al.[10] In future research, test cases with extensive experimental data will be tackled, so that a more in-depth validation of the simulations can be performed.

Acknowledgments

The authors acknowledge the Fund of Scientific Research–Flanders (Belgium) (FWO-Vlaanderen) for financial support through project No. G.0070.03.

Notation

a_w = wall absorptivity
$C_{1\varepsilon}$ = RNG $k - \varepsilon$ model parameter
$C_{2\varepsilon}$ = RNG $k - \varepsilon$ model parameter
C_μ = RNG $k - \varepsilon$ model parameter
C_p = specific heat at constant pressure [J/(kg K^{-1})]
$C_{j,r}$ = molar concentration of species j in reaction r (mol/m^3)
D = molecular diffusivity (m^2/s)
D_t = turbulent diffusivity (m^2/s)
D_{ij} = binary diffusion coefficient for species i and j (m^2/s)
E = total energy per unit mass, $E = h + 0.5u_i + k$ (J/kg)
g_j = component of the gravitational vector in the j direction (m/s^2)
H = mean static enthalpy per unit mass (J/kg)
h_j^0 = enthalpy of formation of species j (J/kg)
I = radiation intensity (W/m^2)
K = turbulent kinetic energy per unit mass (m^2/s^2)
$k_{f,r}$ = forward rate constant for reaction r
$k_{b,r}$ = backward rate constant for reaction r
N_R = number of chemical reactions
N_r = number of chemical species in reaction r
G = incident radiation (W/m^2)
G_k = production of turbulent kinetic energy by velocity gradient (W/m^3)
G_b = production of turbulent kinetic energy by buoyancy (W/m^3)
Pr_t = turbulent Prandtl number
q_r = net radiative heat transfer rate (J/s)
$\vec{r}$ = position vector
R = universal gas constant, $R = 8.314$ [J/(mol K)]
R_i = volumetric rate of creation of species i [mol/(m^3 s)]
S = path length (m)
S_{ij} = mean strain rate tensor
S_{chem} = chemical source term in the energy equation (W/m^3)
S_{rad} = radiation source term in the energy equation (W/m^3)
$\vec{s}$ = direction vector
Sc_t = turbulent Schmidt number

T = temperature (K)
u, v, w = velocity component in the x, y and z direction (m/s)
u_i = velocity component in the ith direction (m/s)
v = kinematic viscosity (m^2/s)
$v'_{i,r}$ = stoichiometric coefficient for reactant i in reaction r
$v''_{i,r}$ = stoichiometric coefficient for product i in reaction r
Y_i = mass fraction of species i

Greek letters

α_ε = RNG $k - \varepsilon$ model parameter
α_k = RNG $k - \varepsilon$ model parameter
β = RNG $k - \varepsilon$ model parameter
ε = dissipation rate of turbulent kinetic energy per unit mass (m^2/s^3) and emissivity
ε_w = wall emissivity
η = ratio of turbulence to mean shear time scale
η_0 = RNG $k - \varepsilon$ model parameter
$\eta'_{j,r}$ = forward rate exponent for each species j in reaction r
$\eta''_{j,r}$ = backward rate exponent for each species j in reaction r
κ = absorption coefficient
λ = laminar thermal conductivity [W/(m K^{-1})]
λ_t = turbulent thermal conductivity [W/(m K^{-1})]
λ_{eff} = effective thermal conductivity [W/(m K^{-1})]
μ = molecular viscosity [kg/(m s^{-1})]
μ_t = turbulent viscosity [kg/(m s^{-1})]
μ_{eff} = effective viscosity [kg/(m s^{-1})]
ξ^* = characteristic length scale of the fine structures (m)
ρ = mean density (kg/m^3)
ρ_{mix} = mixture density (kg/m^3)
σ = Stefan-Boltzmann constant [5.672×10^{-8} W/(m^2 K^4)] and variance
τ^* = characteristic time scale of the fine structures (s)
$\sim$ = Favre average
$''$ = Favre fluctuation

Literature Cited

1. Heynderickx GJ, Oprins AJM, Marin GB, Dick E. Three-dimensional flow patterns in cracking furnaces with long flame burners. *AIChE J*. 2001;47:369–387.
2. Oprins AJM, Heynderickx GJ, Marin GB. Three-dimensional asymmetric flow patterns and temperature fields in cracking furnaces. *Ind Eng Chem Res*. 2001;40:5087–5094.
3. Oprins AJM, Heynderickx GJ. Calculation of three-dimensional flow and pressure fields in cracking furnaces. *Chem Eng Sci*. 2003;58: 4883–4893.
4. Ertesvåg IS, Magnussen BF. The eddy dissipation turbulence energy cascade model. *Combust Sci Technol*. 2000;159:213–236.
5. Stefanidis GD, Merci B, Heynderickx GJ, Marin GB. CFD simulations of steam cracking furnaces using detailed combustion mechanisms. *Comput Chem Eng*. 2006;30:635–649.
6. Borghi R. Mise au point sur la structure des flammes turbulentes. *J Chim Phys*. 1984;81:361–370.
7. Peters N. *Turbulent Combustion*. Cambridge, UK: Cambridge University Press, 2000:33.
8. Poinsot T, Veynante D. *Theoretical and Numerical Combustion*. Philadelphia: RT Edwards, Inc., 2005.
9. Magnussen BF. On the structure of turbulence and a generalized eddy dissipation concept for chemical reaction in turbulent flow. In *19th AIAA Meeting*, St. Louis, 1981.
10. Habibi A, Merci B, Heynderickx G. Impact of radiation models in CFD simulation of steam cracking furnaces. *Comput Chem Eng*. In press.
11. Cheng P. Two-dimensional radiating gas flow by a moment method. *AIAA J*. 1964;2:1662–1664.
12. Siegel R, Howell JR. *Thermal Radiation Heat Transfer*. Washington DC: Hemisphere Publishing Corporation, 1992.
13. Modest MF. *Radiative Heat Transfer*. 2nd edition. New York: Academic Press, 2003.
14. Rosseland S. *Theoretical Astrophysics*. London: Oxford University Press/Clarendon, 1936.
15. Heynderickx GJ, Froment GF. Simulation and comparison of the run length of and ethane cracking furnace with reactor tubes of circular and elliptical cross section. *Ind Eng Chem Res*. 1998;37:914–922.
16. Yakhot V, Orszag SA, Thangam S, Gatski TB, Speziale CG. Development of turbulence models for shear flows by a double expansion technique. *Phys Fluids A*. 1992;4:1510–1520.
17. Launder BE, Spalding DB. The numerical computation of turbulent flows. *Comput Meth Appl Mech Eng*. 1974;3:269–289.
18. Correa SM. Turbulence-chemistry interactions in the intermediate regime of premixed combustion. *Combust Flame*. 1993;93:41–60.
19. Gran IR, Magnussen BF. A numerical study of a bluff-body stabilized diffusion flame, Part 2: Influence of combustion modeling and finite-rate chemistry. *Combust Sci Technol*. 1996;119:191–217.
20. Pope SB. Computationally efficient implementation of combustion chemistry using in situ adaptive tabulstion. *Combust Theor Model*. 1997;1:41–163.
21. Hottel HC, Sarofim AF. *Radiative Transfer*. New York: McGraw Hill, 1967.
22. Smith TF, Shen ZF, Friedman JN. Evaluation of coefficients for the weighted sum of gray gases model. *Trans ASME*. 1982;104:602–608.
23. Janicka J, Kollmann W. The calculation of mean radical concentrations in turbulent diffusion flames. *Combust Flame*. 1982;44:319–336.
24. Hanson RK, Salimian S. Survey of rate constants in H/N/O systems. In: Gardiner WC Jr, editor. *Combustion Chemistry*. New York: Springer-Verlag, 1984:361–421.
25. Westenberg AA. Turbulence modeling for CFD. *Combust Sci Technol*. 1971;4:59–67.
26. Drake MC, Correa SM, Pitz RW, Shyy W, Fenimore CP. Super equilibrium and thermal nitric oxide formation in turbulent diffusion flames. *Combust Flame*. 1987;69:347–365.
27. De Soete GG. Overall reaction rates of NO and N2 formation from fuel nitrogen. *Proc Combust Inst*. 1975;15:1093–1102.
28. Kandamby N, Lazopoulos G, Lockwood FC, Pereira A, Vigevano L. Mathematical Modeling of NO_x Emission Reduction by the use of Reburn Technology in Utility Boilers. In *ASME Int. Joint Power Generation Conf. Exhibition*, Houston, TX, 1996.
29. Pereira A, Antifora A, Sala M, Vigevano L. NO_x emissions in combustion systems of coal fired furnaces with a reducing environment: predictions and measurements. In *4th Int. Conf. Technol. Combust. Clean Environment*, Lisbon, Portugal, 1997.
30. Murthy JY, Mathur SR. A finite volume method for radiative heat transfer using unstructured meshes, AIAA-98-0860. Lebanon, NH: Fluent Inc., 1998.
31. Fluent 6.2 User's Guide. Lebanon, NH: Fluent Inc., 2005.
32. Patankar SV. *Numerical Heat Transfer and Fluid Flow*. Washington: McGraw Hill, 1980.
33. Byggstϕyl S, Magnussen BF. A model for flame extinction in turbulent flow. In *4th Symp. Turbul. Shear Flows*, Karlsruhe, 1983.

Manuscript received Jan. 17, 2007, and revision received May 21, 2007.